Origins of Rydberg-Atom Electrometer Transient Response and Its Impact on Radio-Frequency Pulse Sensing

Stephanie M. Bohaichuk,[†] Donald Booth, Kent Nickerson, Harry Tai, and James P. Shaffer[*]

Quantum Valley Ideas Laboratories, 485 Wes Graham Way, Waterloo, Ontario N2L 6R2, Canada

Rydberg atoms show significant promise as the basis for highly sensitive detectors of continuous radio-frequency (rf) electric fields (E fields). Here, we study their time-dependent response to pulse-modulated rf E fields at 19.4 GHz using a cesium vapor cell at room temperature. We use density-matrix simulations to explain the timescales that shape the transient atomic response under different laser conditions, finding them to be limited by dephasing mechanisms, including transit-time broadening, Rydberg-Rydberg collisions, and ionization. Using a matched filter, we demonstrate the detection of individual pulses with durations from 10 μs down to 50 ns and amplitudes from 15 000 μV cm^{-1} down to about 170 μV cm^{-1}, corresponding to a sensitivity of about 240 nV cm^{-1} Hz$^{-1/2}$. Finally, we highlight the potential of a Rydberg vapor cell as a receiver by detecting pulse trains from a rotating emitter on a simulated passing aircraft.

I. INTRODUCTION

Rydberg atoms form the basis for several quantum technologies due to their uniformity, stability, and well-known properties [1]. For alkali atoms, like cesium (Cs), light can optically excite the outer electron into a Rydberg state that is sensitive to the presence of other atoms and external electric fields. There are many available excited states that offer significant tunability of Rydberg-atom properties. Rydberg atoms are of significant interest for neutral-atom quantum simulators [2,3], neutral-atom quantum computing [4,5], single-photon sources [6], and radio-frequency electrometry [7–11].

In Rydberg-atom-based sensors, quantum interference between laser fields resonant with atomic transitions generates optical transmission in an absorbing vapor, termed electromagnetically induced transparency (EIT) [12,13]. The presence of a rf electric field (E field) resonant with another atomic transition disrupts the EIT and changes the optical transmission in proportion to the rf E-field amplitude [7]. These sensors can be self-calibrated and detect electromagnetic fields across a broad MHz-THz frequency range, down to amplitudes of about 1 μV cm^{-1} with a sensitivity of about 1 μV cm^{-1} Hz$^{-1/2}$ [14–16], which can be improved to <55 nV cm^{-1} Hz$^{-1/2}$ by adding an auxiliary rf E field [17]. Small dielectric vapor cells ($\lesssim$30 mm^3) minimally perturb the E field and enable imaging with subwavelength spatial resolution [10,18,19].

While Rydberg sensors are predominantly studied for sensing the amplitude of continuous-wave rf E fields, temporal dynamics can occur at submicrosecond timescales [20,21]. This makes Rydberg sensors interesting for detecting modulated rf E fields [21–25]. Furthermore, the polarization or phase of the rf E field can be detected [17,26,27].

We study the atomic response to pulse-modulated rf E fields to demonstrate the sensing of individual rf pulses of the type used in communications and radar and to evaluate limitations on the signal-to-noise ratio (SNR) and timing accuracy. Performance greatly improves by applying a matched filter tailored to the atomic response, despite the atomic system's nonlinearity and time variance. We detect rf E fields down to about 170 μV cm^{-1}, corresponding to a sensitivity of about 240 nV cm^{-1} Hz$^{-1/2}$ without the need for an auxiliary rf E field or additional modulation. Finally, we demonstrate the use of a Rydberg sensor as a radar receiver for pulses emitted by a passing aircraft.

II. EXPERIMENTAL SETUP AND RF-PULSE RESPONSE

To study the response of Rydberg atoms to a pulsed rf E field, we use a 3-cm-long by 1-cm-square glass-blown cell filled with cesium vapor at room temperature. EIT in the vapor cell is generated using spatially overlapped counterpropagating infrared probe (852.35 nm) and green coupling (509.31 nm) laser beams with about 140- and 160-μm $1/e^2$ radii, respectively. These are resonant with transitions between atomic states in the ladder system shown in Fig. 1(a) and are both polarized linearly, parallel to each other. In all measurements, the probe laser is

_____
[*]jshaffer@qvil.ca
[†]sbohaichuk@qvil.ca

offset locked to the Cs $F = 4$ to $F' = 5$ D2 transition using an external Fabry-Perot cavity and the Pound-Drever-Hall technique. The coupling laser is either scanned in frequency to measure steady-state EIT or offset locked, using the same cavity, to resonance to measure a pulsed-rf E field. The laser spectral bandwidths are <100 kHz. Changes in the transmission of the probe laser through the vapor cell (ΔT) are detected using an avalanche photodetector with a bandwidth of 10 MHz. The detector output is fed into an oscilloscope, or a field-programmable gate array (FPGA) for further processing using a matched filter.

The rf pulses are applied using the pulse modulation of a synthesizer, with rise and fall times of <80 ns, output to a rf horn antenna with a gain of about 20 dB placed about 30 cm from the cell. Unless otherwise specified, we use a frequency of 19.4 GHz, which couples the $55D_{5/2}$ and $53F_{7/2}$ Rydberg states of Cs, with a pulse repetition rate of 5 kHz. The rf E field is linearly polarized, perpendicular to the laser polarizations and parallel to their propagation directions.

Figure 1(b) shows EIT measured from the vapor cell with no rf E field applied (blue curve) as the coupling

laser is scanned over the Cs $6P_{3/2} \leftrightarrow 55D_{5/2}$ transition. The full width at half-maximum (FWHM) of the EIT peak under these laser conditions is about 11 MHz and increases with the probe and coupling Rabi frequencies, Ω_P and Ω_C, respectively. Upon application of a continuous-wave 19.4-GHz rf E field, Autler-Townes splitting of the EIT peak is observed, as shown in red and orange for two different field strengths. The slight asymmetry in peak height for the orange trace is an example of a weak background dc E field present in the vapor cell. The peak splitting is given by $\Delta \nu = E\mu_{34}/h$, where $\mu_{34} = 6294.3ea_0$ is the dipole moment of the $55D_{5/2} \leftrightarrow 53F_{7/2}$ transition, h is Planck's constant, and E is the amplitude of the rf E field. If the rf E-field strength is very weak then splitting does not occur, but the amplitude of the on-resonance EIT signal decreases in what we refer to as the amplitude regime. In between these limits, the peaks split but remain partially overlapped.

In the Autler-Townes splitting regime, we can directly extract the rf E-field amplitude at the vapor cell using the known atomic dipole moment for the rf transition and the measured spectral splitting of the Autler-Townes peaks as the coupling laser is scanned over resonance. In the
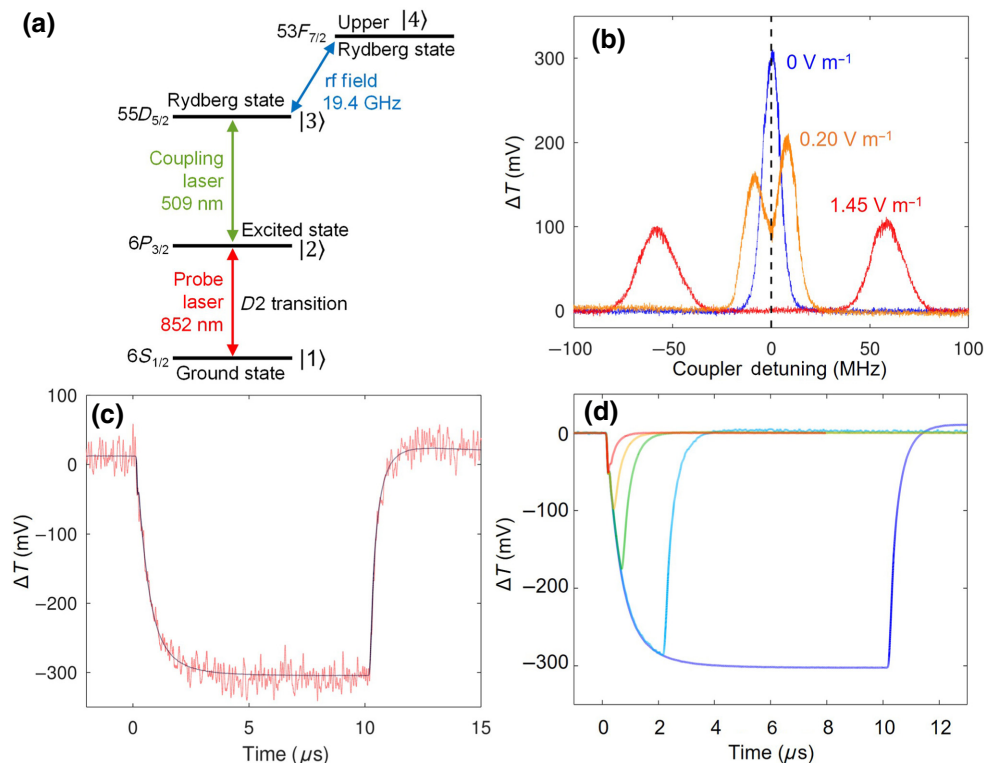
FIG. 1. (a) Energy-level diagram for the experimental cesium system. (b) EIT peak (blue) obtained as the coupling laser is scanned across resonance. Autler-Townes splitting of the peak is shown in red and orange for two different continuous-wave rf E fields. To measure rf pulses, the coupling laser is locked on resonance (dashed line). (c) Transient atomic response to a 10-μs rf pulse, which is measured as a change in transmission of the probe laser, with both a single trace (red) and one averaged over 10^4 cycles (purple) for a rf E field of 1.45 V m^{-1}, corresponding to $\Omega_{rf} = 2\pi \times 117$ MHz. (d) Averaged atomic responses to rf pulses of varying durations, ranging from 50 ns to 10 μs. Shorter pulses do not reach the full steady-state depth and, as a result, are harder to detect. $\Omega_P = 2\pi \times 3.5$ MHz and $\Omega_C = 2\pi \times 2.1$ MHz.

amplitude regime, where the EIT peak splitting is not discernable in response to weak rf E fields, <0.1 V m^{-1}, we extrapolate the rf E-field strength at the atoms in the vapor cell using a calibration factor. This calibration factor converts the nominal output E field of the rf generator to an E field received at the vapor cell, based on the linearity of the generator's attenuator and the dipole moment of the Rydberg-Rydberg transition. We determine this factor by measuring the splitting of the EIT peaks in response to continuous-wave rf E fields of various strengths within the Autler-Townes regime in comparison with the nominal rf-generator output.

To detect a rf pulse, the coupling and probe lasers are locked on resonance [vertical dashed line in Fig. 1(b)]. Upon application of a rf pulse, the EIT peak splits, resulting in a large drop in transmission, which is detected as a pulse, as shown in Fig. 1(c). The atomic response approximates the shape of the rf-pulse envelope but has slower leading and trailing edges, which each take about 2 μs to reach steady state after an initial rapid <100-ns transient.

In Fig. 1(d), we examine the atomic response to various rf-pulse durations down to 50 ns, which is the limit of the rf generator's capabilities. The pulses are comprised of the same atomic timescales, but the total depth is reduced as the rf pulse is shortened, resulting in a degraded SNR when detecting single pulses, as the atoms are unable to respond quickly enough to sub-2-μs pulses to reach a steady-state optical transmission. Despite this, it remains possible to detect very short pulses due to the rapid decrease in optical transmission on the leading edge.

III. MODELING AND ORIGINS OF ATOMIC TIMESCALES

To understand the origins of the atomic timescales, we perform density-matrix calculations, which follow the time-dependent master equation:

$$\dot{\rho} = \frac{2\pi i}{h}[\rho, H] + \mathcal{L}(\rho), \qquad (1)$$

where H is the Hamiltonian of the system, ρ is the density matrix, h is Planck's constant, and $\mathcal{L}$ is the Lindblad operator, which describes decays and dephasing [28,29]. The levels in the model system correspond to those shown in Fig. 1(a), with $|1\rangle$ referring to the ground state; $|2\rangle$ to the intermediate excited state; $|3\rangle$ to the lower Rydberg excited state; and $|4\rangle$ to the Rydberg excited state, which is coupled to $|3\rangle$ by the time-dependent rf Rabi frequency. We add a fifth level, $|5\rangle$, as a dark state to represent atomic states that are not optically coupled to the primary system. This level better models the pulse timescales at higher Rydberg populations and coupling optical Rabi frequencies but is not necessary at low Rydberg populations where pulse detection is typically ideal. We describe the Hamiltonian of this system in the interaction picture by

$$H = \frac{h}{2\pi} \begin{pmatrix} 0 & \frac{\Omega_P}{2} & 0 & 0 & 0 \\ \frac{\Omega_P}{2} & -\Delta_2 & \frac{\Omega_C}{2} & 0 & 0 \\ 0 & \frac{\Omega_C}{2} & -\Delta_3 & \frac{\Omega_{\mathrm{rf}}(t)}{2} & 0 \\ 0 & 0 & \frac{\Omega_{\mathrm{rf}}(t)}{2} & -\Delta_4 & 0 \\ 0 & 0 & 0 & 0 & 0 \end{pmatrix}. \qquad (2)$$

Ω_P, Ω_C, and $\Omega_{\mathrm{rf}}(t)$ are the Rabi frequencies of the probe laser, the coupling laser, and the rf E field, respectively. The atomic dipole moments used to determine the optical Rabi frequencies are averaged over the accessible hyperfine transitions in our setup, taking into account the laser polarizations. The rf E field is initially *off* ($\Omega_{\mathrm{rf}} = 0$) for the first 10 μs, so that the simulation reaches equilibrium, then the rf E field is pulsed on for a 10-μs duration, with a 25-ns rise and fall time. Detuning of the $|2\rangle$ state is given by $\Delta_2 = -\Delta_P + k_P v$ and detuning of the $|3\rangle$ state by $\Delta_3 = -\Delta_P - \Delta_C + (k_P - k_C)v$. Here, both lasers are locked on resonance, so $\Delta_P = \Delta_C = 0$. k_P and k_C are the wavevectors of the probe and coupling lasers, respectively, while v is the atomic velocity along the direction of the probe laser used to account for Doppler shifts. We obtain Doppler-averaged values by integrating v over the Boltzmann distribution:

$$\rho_{21} = \int \sqrt{\frac{m}{2\pi k_B T_C}} \exp\left(-\frac{mv^2}{2k_B T_C}\right) \rho_{21}(v) dv, \qquad (3)$$

where T_C is the vapor cell temperature; m the atomic mass of the alkali atom used, here ^{133}Cs; and k_B is the Boltzmann constant. We use the imaginary part of the density-matrix element, ρ_{21}, which is proportional to the absorption coefficient, α, to obtain the response of the vapor. This closely approximates the total change in intensity of the probe laser in the vapor cell under weak-absorption conditions, as an absolute value for total absorption can be difficult to model due to uncertainties in the atom-number density; optical losses, including reflections and absorption due to the vapor cell walls and downstream optical components; and detector sensitivity and gain.

In the Lindblad operator, we include $\Gamma_{21} = 2\pi \times 5.2$ MHz as the well-known decay rate from $6P_{3/2}$ to $6S_{1/2}$ [30], and $\Gamma_{32} = 2\pi \times 10.4$ kHz as a radiative decay rate for the Rydberg state to the excited state. $\Gamma_{31} = \Gamma_{41} = \Gamma_{51}$ represents a transit time of atoms through our laser beams.

We fit our model to an experimental pulse shape obtained at low optical Rabi frequencies, as shown in Fig. 2(a), using a differential evolution routine, which belongs to the lmfit package in PYTHON [31,32]. This minimizes the sum of squared residuals between the model and experimental pulse using a stochastic search due to the nonlinear nature of the problem. We expect the probe and coupling Rabi frequencies to be $2\pi \times 2.0$ MHz
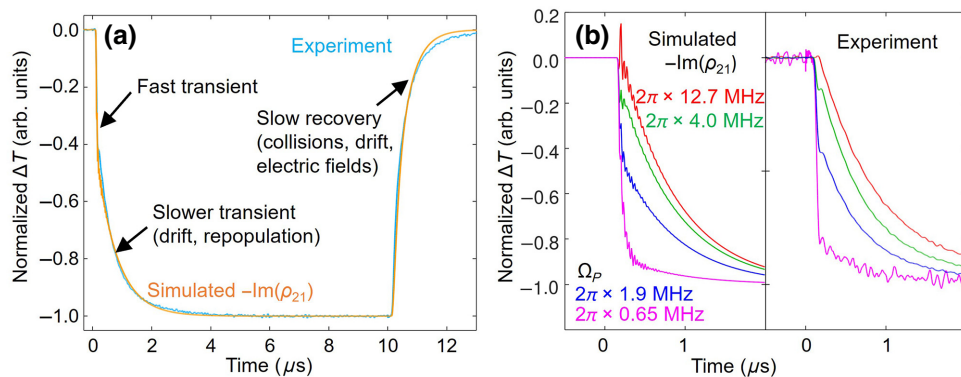
FIG. 2. (a) Experimental atomic response to a 10-μs rf pulse (blue) compared to one simulated with a density-matrix model (orange). Pulses consist of several atomic timescales, which are labeled by their origins. $\Omega_P = 2\pi \times 1.9$ MHz, $\Omega_C = 2\pi \times 0.7$ MHz, and $\Omega_{\mathrm{rf}} = 2\pi \times 60$ MHz. (b) Changes to the leading edge of the atomic response with the probe power, shown in both modeling (left panel) and experiment (right panel). $\Omega_C = 2\pi \times 0.7$ MHz, $\Omega_{\mathrm{rf}} = 2\pi \times 60$ MHz.

and $2\pi \times 0.6$ MHz, respectively, but allow them to vary slightly within experimental bounds of $2\pi \times 1.0$–2.5 MHz and $2\pi \times 0.5$–0.75 MHz, accounting for variation and uncertainty in the beam size and power along the 3-cm cell length. We similarly allow the transit-time rate to vary within the bounds $2\pi \times 200$–600 kHz. As shown in Fig. 2(a), resulting fit values of $\Omega_P = 2\pi \times 1.9$ MHz, $\Omega_C = 2\pi \times 0.7$ MHz, and a transit time of $2\pi \times 223$ kHz reproduce the pulse shape well without the need for a dark state (i.e., $\Gamma_{35} = 0$). Standard errors reported by the fit (1σ error bars from an estimated covariance matrix) are $<0.2\%$ for all parameters but may be underestimated due to the model nonlinearity and the nonzero correlations between parameters.

The pulse leading edge consists of two timescales: a sharp decrease in transmission occurring over about 100 ns, followed by a slower exponential reduction in transmission over a few microseconds. During the initial transient, the two-level system on the *D*2 transition rapidly

drives itself to equilibrium, based on the populations in the $6P_{3/2}$ and $6S_{1/2}$ states and their coherences, in response to effective alteration of the EIT by the rf *E* field. The depth of the transient diminishes as Ω_P increases, as shown in Fig. 2(b). Here, we run the model using the same fit values of Ω_C and the transit time from Fig. 2(a), while Ω_P is scaled from the fit value according to the measured probe laser power. Moving further from the weak-probe limit to higher Ω_P results in more atoms initially populating the $6P_{3/2}$ state and less change due to the presence or absence of the coupling laser, so that when the rf *E* field is turned on there is less change in $6P_{3/2}$ population. At larger Ω_P, the pulse is, therefore, dominated by the slower time constant. For fast timing applications, it is advantageous to use lower Ω_P where the sharp transient is deeper.

The subsequent slower dynamics are explained by the repopulation of the interaction region in the vapor cell due to atomic motion, as set by the transit time of atoms through the beam and the populations of Rydberg and dark
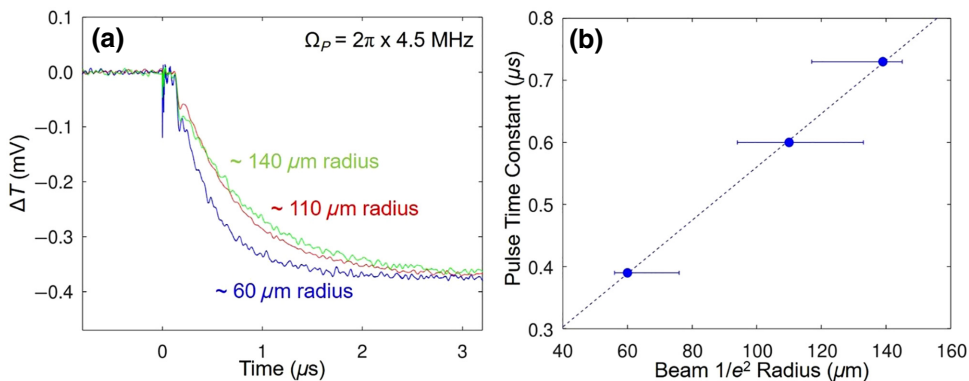
FIG. 3. Effects of transit time on experimental pulse shape. (a) Increasing the probe-beam radius, which is smaller than the coupling-laser beam, slows the atomic response at the leading edge of the pulse. Constant Rabi frequency is maintained by increasing the probe laser power accordingly. (b) Time constant extracted from an exponential fit to the leading edge of the pulse scales linearly with the probe-beam radius.

states. Prior to the rf pulse, EIT produces a steady-state Rydberg population. When Rydberg populations are high, a fraction of these end up in a dark state due to Rydberg-Rydberg collisions, radiative decay, and blackbody radiation and ionization and are unable to participate in the optical dynamics. Once the rf pulse is turned on, disrupting EIT, creation of the Rydberg population is hindered, as is any associated dark-state population. The atoms present in the upper Rydberg state, which becomes populated when the rf is on; the lower Rydberg state; and the dark state slowly drift out of the laser beams and are replaced by ground-state atoms, at a rate set by the transit time. An exponential fit to the portion of experimental pulses after the initial transient yields an effective time constant that decreases linearly when we decrease the probe-laser-beam diameter and, therefore, the transit time, as shown in Fig. 3. The initial <100-ns transient present on the leading edge of pulses is unaffected by the laser-beam size and transit time, to within the bandwidth resolution of the photodetector. Given that the transit time dominates the overall atomic response time, the use of large laser beams may not lead to

an increased SNR when detecting short pulses, as it is not conducive to quickly reaching equilibrium depth.

The recovery of the pulse's trailing edge can be longer than the dynamics of the leading edge and at higher laser powers often displays enhanced transmission, i.e., long-lasting overshoots. We attribute this, in part, to collisional-dependent ionization and electric field effects in the vapor cell, which take considerably more time to re-equilibrate after changes to the Rydberg population that occur during and shortly after the pulse. As shown in Figs. 4(a) and 4(b), these effects can last up to about 100 μs. Conditions that increase the Rydberg-atom population, such as increased coupling-laser power [Figs. 4(a) and 4(b)], tend to increase the presence of overshoots and long transients on the tail due to increased collisions and ion generation. We also find that the long-transient tail depends on the position of the lasers relative to the vapor cell walls, as shown in Fig. 4(c), suggesting that any background electric fields in the vapor cell can be influential. Such a background dc electric field is typically stronger closer to the cell walls due to surface charges. The total depth of the pulse changes as the
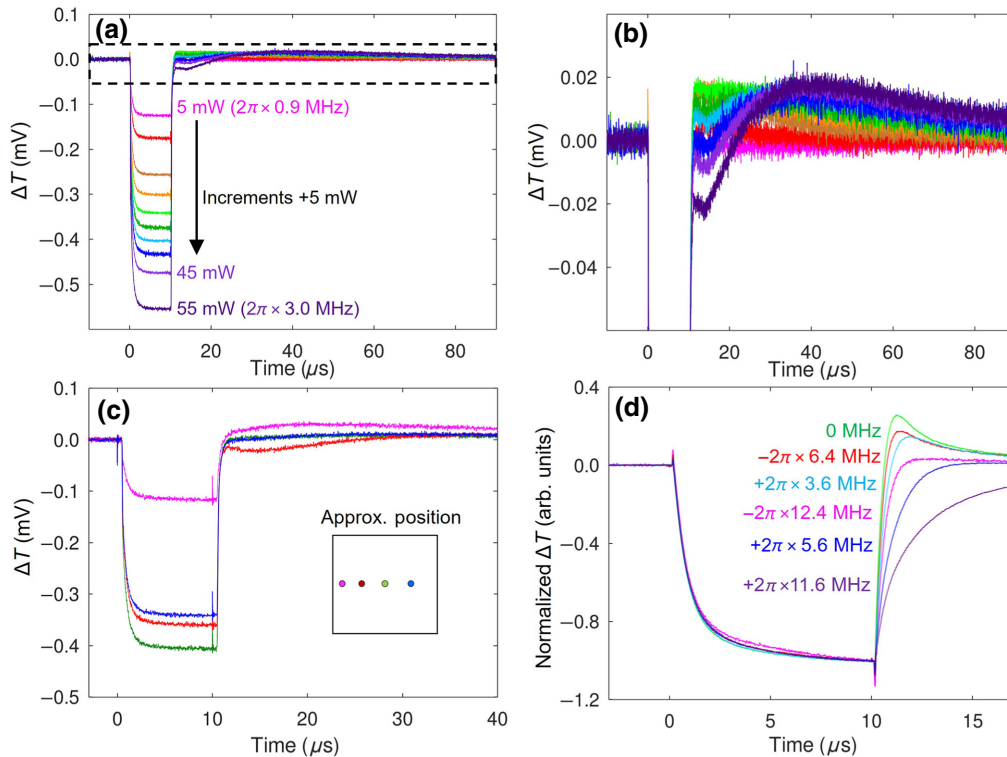
FIG. 4. Experimental electric field effects. (a) Trailing edge of the pulse shows stronger overshoots at higher coupling-laser Rabi frequencies, the effects of which can linger over many tens of microseconds. $\Omega_P = 2\pi \times 1.8$ MHz (b) Magnification of the dashed box in (a). (c) While the shape of the leading edge of the pulse does not change with the laser-beam positions relative to the vapor cell walls, the shape of the trailing edge does. Inset shows an approximate location for the laser beams within the 1×1 cm^2 face of the vapor cell, with the lasers going in and out of the page. $\Omega_P = 2\pi \times 1.8$ MHz, $\Omega_C = 2\pi \times 2.6$ MHz. (d) Coupling-laser detuning has a strong impact on the tail of the experimental response to a rf pulse. $\Omega_P = 2\pi \times 10.2$ MHz, $\Omega_C = 2\pi \times 2.2$ MHz, $\Omega_{rf} = 2\pi \times 119$ MHz. All experimental pulses are averaged $>10^3$ cycles.
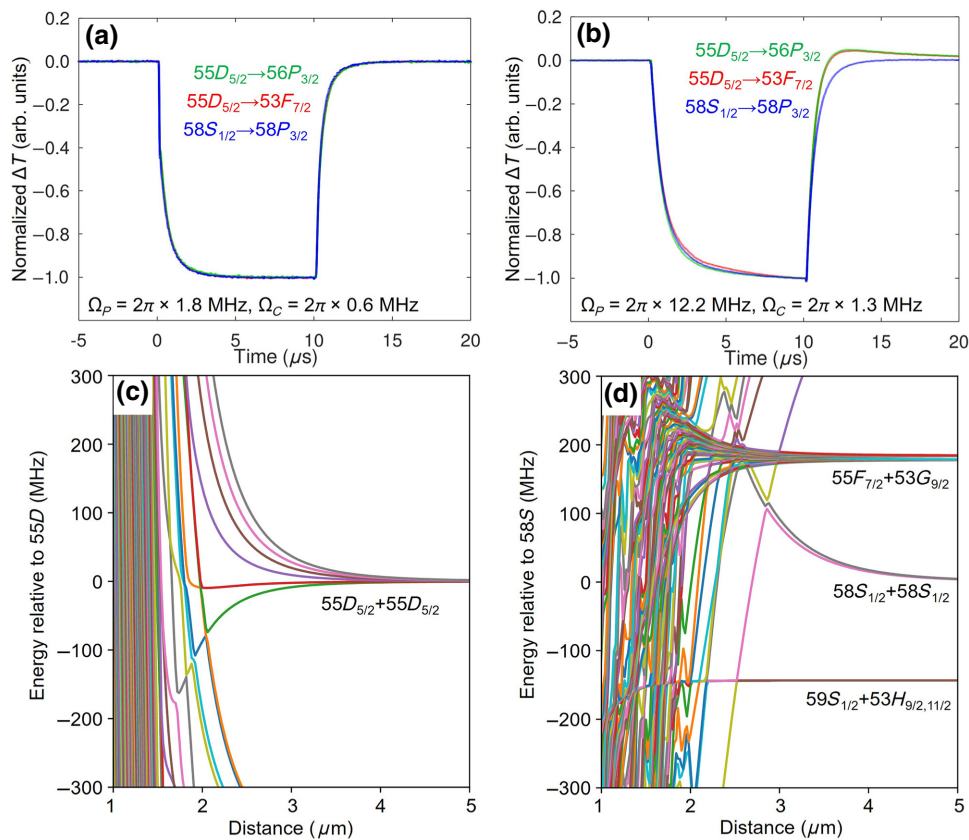
FIG. 5.   Effects of atomic transition choice on experimental pulse shape. (a) At low optical Rabi frequencies, changes to the Rydberg transitions have no visible impact on the leading edge of the atomic response. (b) At higher laser powers, the choice of Rydberg transitions has a minimal effect on the leading edge of the pulse but does affect the trailing edge, likely due to the varying collisional rates and polarizability among states. $\Omega_{\rm rf} = 2\pi \times 60$ MHz. Pairwise interaction potentials calculated for (c) $55D_{5/2}$ and nearby Rydberg states and (d) $58S_{1/2}$ and nearby Rydberg states. $55D_{5/2}$ pair states show some attractive interaction potentials that lead to collisions, unlike the $58S_{1/2}$ pair states, which are all repulsive.

laser positions are shifted, primarily due to changes in optical transmission through the glass faces of the vapor cell. Finally, as shown in Fig. 4(d), the shape of the trailing edge is highly sensitive to the detuning of the coupling laser. Detuning the coupling laser causes excitations of Rydberg-atom pairs with different forces of attraction or repulsion, i.e., gradients of pair potential curves, resulting in different collisional and ionization rates, depending on the amount and sign of detuning.

Since pulse recovery is dominated by collisions and ionization, then we also expect it to depend on the choice of Rydberg transitions used, which we investigate in Fig. 5. In addition to the $55D_{5/2} \leftrightarrow 53F_{7/2}$ transition (K-band 19.40-GHz microwaves), we examine the $55D_{5/2} \leftrightarrow 56P_{3/2}$ transition (C-band 4.2-GHz microwaves) and the $58S_{1/2} \leftrightarrow 58P_{3/2}$ transition (K-band 18.9-GHz microwaves, with the coupling laser shifted to 509.26 nm) at large rf E fields when the EIT peaks are fully split. For the C-band measurements, we change to a rf horn antenna designed for 4 GHz operation, placed about 40 cm from the

cell. However, we maintain fixed rf and optical Rabi frequencies for all three transitions. Qualitatively, the pulse shape is identical for all the different choices of atomic transitions at low Rabi frequencies [i.e., low laser powers shown in Fig. 5(a)] when Rydberg collision and ionization rates are low, which is optimal for weak-rf-pulse detection. We therefore expect to be able to sense pulses with similar temporal accuracy using different atomic states, albeit with different degrees of sensitivity and pulse depth due to the slightly different dipole moments of the transitions, μ_{34}.

At higher laser powers in Fig. 5(b), we observe different degrees of overshoot on the trailing edge of the pulses, though the leading edge remains the same. The $58S_{1/2} \leftrightarrow 58P_{3/2}$ transition has equal pre- and postpulse transmission levels, apparently avoiding significant collisional and electric field effects, unlike the other transitions. To understand this, we calculate pair-wise potentials for the $58S_{1/2}$ and $55D_{5/2}$ Rydberg pair states shown in Figs. 5(c) and 5(d). These calculations include both dipole and quadrupole interactions [33]. All of the interaction potentials for the $58S_{1/2}$ state are repulsive, and the

steep avoided crossings shown are unlikely to result in transitions due to extremely low Landau-Zener curve-crossing probabilities. The crossing of the $58S_{1/2}$ pair state with the nearby $55F_{7/2} + 53G_{9/2}$ is not directly allowed by either quadrupole or dipole interactions. In contrast, the $55D_{5/2}$ pair-state potentials include attractive potential curves that can more easily lead to state-changing collisions. Furthermore, we calculate the polarizability of the $55D_{5/2}, m_J = 5/2$, and $58S_{1/2}, m_J = 1/2$, states to be -2800 and 155 MHz/(V/cm)^2, respectively. Given the significantly lower polarizability of the $58S_{1/2}$ state, we expect a lower sensitivity to Stark shifts driven by ionization and electric fields in the vapor cell. Since $58S_{1/2}$ is more immune to both collisional and ionization effects, we see far less slow overshoot on the recovery of the pulse. Data showing that the results for the $56P_{3/2}$ and $53F_{7/2}$ Rydberg states are effectively identical indicate that the rf-coupled upper-Rydberg-state $|4\rangle$ has little role in shaping the pulse and populating the dark state. The atomic response is primarily shaped by the population accumulated before the pulse turns *on*, when the rf is *off* and no upper-state $|4\rangle$ population is present. Once the rf pulse is applied, population can be produced in $|4\rangle$ but does not meaningfully contribute to any dark-state population because of the short time over which it is coupled to the optical system. However, neglecting the $|4\rangle$ population is not accurate for all pulse lengths and repetition rates.

All of these effects highlight that the slow-trailing edge of the pulse can be sensitive to factors such as collisions, generation of ions, and background electric fields in the vapor cell. In general, it is preferred to perform pulse detection at low optical powers where these effects are minimized. However, here, we add a dark-state generation rate, Γ_{35}, to our model to attempt to capture some of these effects. Γ_{35} represents a dark-state generation rate for atoms and/or ions, arising primarily through Rydberg-Rydberg collisions; this is important under optical conditions that generate high-Rydberg-state populations. We can obtain an estimated value for this rate using [34]

$$\Gamma_{35} \sim \eta N_g \rho_{33} \bar{v} \sigma, \qquad (4)$$

where $N_g \sim 3 \times 10^{16}$ m^{-3} is the number density of Cs atoms in the vapor cell at room temperature, $\rho_{33} \sim 0.1\%$ is an approximate population in Rydberg-state $|3\rangle$ for our typical experimental conditions, $\bar{v} = 219$ m/s is the average velocity of atoms, and $\sigma = \pi R_{nn}^2$ is the cross section for Rydberg-Rydberg collisions. Using pair-wise interaction potentials for two $55D_{5/2}$-state atoms [33], we estimate the internuclear distance at which a collision interaction occurs to be $R_{nn} \sim 7$ μm, corresponding to a shift in the energy levels equivalent to the laser spectral bandwidth. If we assume that one in every ten collisions produces an atom or ion in a dark state, $\eta = 0.1$, then we obtain an estimated collision rate on the order of $\Gamma_{35} \sim 2\pi \times 100$ kHz.

Note that the shifted atoms are effectively in a dark state as well, due to blockade, but Doppler shifts also play a role in determining which atoms participate in the EIT process.

We also expect there to be some ions generated in the vapor cell due to, for example, Penning ionization or blackbody radiation. At the typical Rydberg densities we work with, blackbody-radiation-induced ionization rates are expected to be several hundred Hz [35], while Penning ionization rates are lower [36,37]. While the generation rate of ions is thus expected to be very low, their long-range interactions can still have an impact on atoms in a Rydberg state. Here, we provide simple estimates for the plausibility of ionization influencing the pulse shape. Based on calculations for the $55D_{5/2}$ state [33], we expect that a >10-mV cm^{-1} electric field is needed to produce an appreciable Stark shift of >100 kHz. We estimate that a Rydberg atom must, therefore, be within $R_{ion} \sim 38$ μm of the ion to experience the required electric field, given the $1/r^2$ dependence of an electric field around a charged particle. Similar to Eq. (4), we can write an approximate rate, Γ_{ion}, for the disturbance of a given Rydberg atom via interaction with an ion, i.e., how often the Rydberg atom ends up within R_{ion} of an ion:

$$\Gamma_{ion} \sim N_g \rho_{ion} \bar{v} \sigma, \qquad (5)$$

where ρ_{ion} is the ion population and $\sigma = \pi R_{ion}^2$ is an estimated cross section for Rydberg-ion interactions. To obtain an ion population in the long time between pulses, when the rf is *off*, we can solve the following rate equation in steady state:

$$\frac{dn_{ion}}{dt} = \rho_{33} N_g G_{ion} - n_{ion} \Gamma_{ti} \sim 0, \qquad (6)$$

where $n_{ion} = \rho_{ion} N_g$ is the number density of ions, Γ_{ti} is the transit time of ions through the interaction region, and G_{ion} is the generation rate of ions from blackbody radiation and Penning ionization. We expect the effective interaction-region diameter to be larger than the laser beams because of the large effective radius of an ion's influence, R_{ion}, which results in a slower transit time, $\Gamma_{ti} \sim 2\pi \times 175$ kHz. Solving Eqs. (5) and (6), we expect roughly 0.2% of Rydberg atoms to end up as ions, resulting in a disturbance rate with an order of magnitude around $\Gamma_{ion} \sim 2\pi \times 150$ kHz, which is similar to our Rydberg-Rydberg collision-rate estimate.

If we run the model in Fig. 2(a) at a higher coupling Rabi frequency, $\Omega_C = 2\pi \times 2.5$ MHz, and therefore, a higher Rydberg population of about 0.2%, then we observe a poor match to corresponding experimental data shown in Fig. 6. For larger Rydberg-state populations, background electric fields in the cell, collisions, and ions may all play a role in the dynamics and contribute to this mismatch. We attempt to capture these
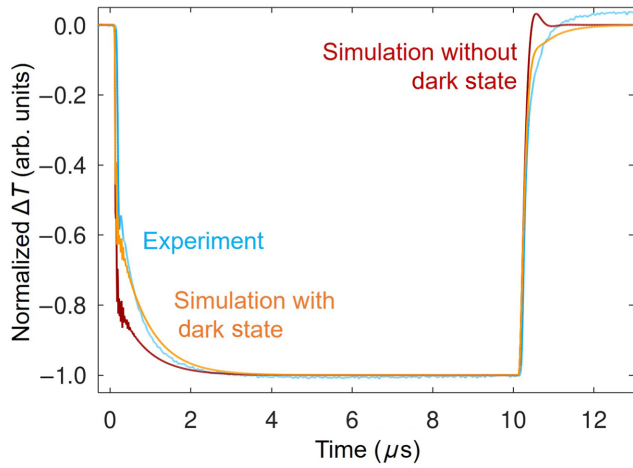
FIG. 6. Experimental atomic response to a 10-μs rf pulse (blue) compared to one simulated with a density-matrix model that does not (red) or does (orange) include the presence of dark-state atoms and/or ions. Under these conditions with higher Rydberg populations, the dark state is needed in the model to better fit both pulse edges. Very long overshoot is present on the tail in experimental data that neither model can capture, likely due to the presence of electric fields and ions, because it is difficult to model their buildup and positions in the vapor cell. $\Omega_P = 2\pi \times 1.9$ MHz, $\Omega_C = 2\pi \times 2.5$ MHz, and $\Omega_{\rm rf} = 2\pi \times 60$ MHz.

effects by including a dark-state-generation rate, Γ_{35}, in our model to fit to experimental data, which we allow to vary from $2\pi \times 0$–1 MHz consistent with the order of magnitude estimates, while fixing the Rabi frequencies and transit time to the previous fit values. The fit results in a value of $\Gamma_{35} = 2\pi \times (680 \pm 3)$ kHz, which significantly improves the pulse shape and reduces the sum of residuals by about 55%. The inclusion of the dark state halves the Rydberg-state population present in the interaction volume prior to the rf pulse and results in a deeper slow transient on the leading edge as accumulated dark-state atoms slowly drift out of the beam due to the finite transit time. The dark state also contributes to dephasing that dampens rapid overshoots on the trailing edge of the pulse, which otherwise arise due to coherent dynamics. However, the inclusion of the dark state does not reproduce the much slower transients and overshoots seen experimentally on pulse recovery. These slower processes are the result of a gradual build-up of charges and, consequently, electric fields in the vapor cell that are difficult to quantitatively model. In general, atomic pulse shapes at even higher optical Rabi frequencies will require higher dark-state-generation rates. These rates must be fit to data to best approximate pulse shape but will be unable to capture the full extent of long-lived collisional and ionization dynamics.

IV. DETECTION OF INDIVIDUAL RF PULSES

Figure 7(a) shows the measured atomic response to 19.4-GHz pulses of different amplitudes, with the corresponding experimental EIT peak splitting from continuous rf E fields shown in the inset. The primary change is the depth of the pulse, as lower rf amplitude leads to reduced peak splitting. To convert a pulse depth to a rf E-field amplitude, prior calibration against several known fields is required, which can be performed with either pulsed or continuous-wave fields. For calibration, we measure the Autler-Townes splitting, and therefore, the rf E field at the atoms, induced by a continuous-wave rf E field at a given power reading on the rf-generator output, and then scale for different power readings using the same apparatus. The depth of the atomic response reaches its maximum once the rf E field is strong enough to fully split the EIT peaks, and any further increases in rf E field will not increase the atomic pulse response depth. Therefore, strong rf E fields cannot be distinguished from pulse amplitude alone.

To improve the detection of weak rf pulses, we apply a matched filter, which is used in many signal-processing applications to extract a known pulse shape from white noise [38]. We implement the matched filter on a FPGA to perform real-time analysis. The output peak corresponds to the time of maximum cross correlation, i.e., best match, of an expected pulse template to a measured noisy waveform. The template is obtained from experimental data recorded under the same laser conditions, averaged over many cycles to reduce noise. A simulated template can be used instead but, given that collisions and cell-dependent electric fields can be nontrivial to accurately capture, better performance of the matched filter is obtained at higher optical powers by using an experimental template. We cannot use the outgoing rf pulse as the expected template, in contrast to many implementations, as the atomic response shape does not match the square rf-pulse envelope due to the finite atomic response time. As the pulse shape varies minimally with rf amplitude, we use the same pulse template at different rf amplitudes. We address the consequences of template-experiment mismatch later. Another difference between traditional receivers and a Rydberg-atom receiver is that we directly couple the FPGA to the sensor without an intermediate filter or amplifier.

Figure 7(b) shows the output of the matched filter applied to individual pulses under the same conditions as in Fig. 7(a). The matched filter significantly suppresses noise, allowing the timing of weaker-amplitude rf pulses to be extracted. The timing extracted by the matched filter is the arrival time of the pulse plus its duration, as determined by the length of the template, which here is 11.1 μs.

As the EIT peak FWHM is strongly influenced by the combination of probe and coupling Rabi frequencies, we
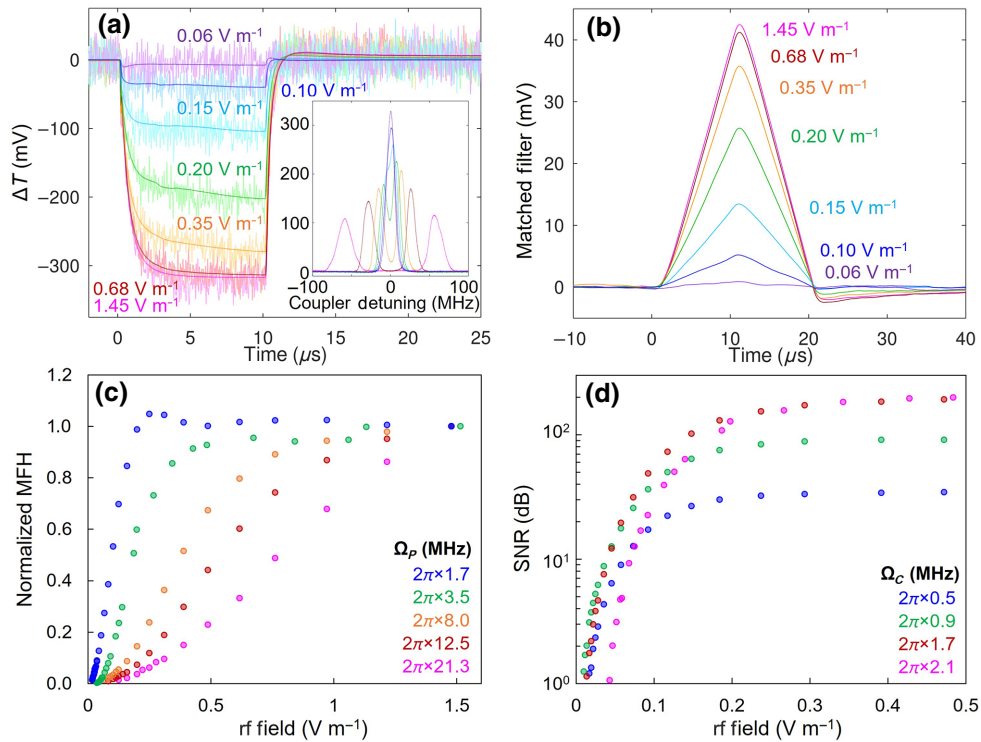
FIG. 7. (a) Experimental atomic responses to a 10-μs rf pulse of various E-field amplitudes, shown as both single traces (faint lines) and traces averaged over 10^4 cycles (darker lines). Inset shows the corresponding Autler-Townes splitting of the EIT peaks in response to a continuous-wave rf E field. $\Omega_P = 2\pi \times 3.5$ MHz, $\Omega_C = 2\pi \times 2.1$ MHz. (b) Output of the matched filter when applied to pulses shown in (a). Peak of the filter output gives the pulse timing. (c) Peak height of the matched-filter signal (MFH) as a function of probe laser power, normalized to the value at full EIT peak splitting and maximum atomic response depth (large-rf E field) at fixed $\Omega_C = 2\pi \times 2.4$ MHz. (d) SNR of the matched filter as the coupling-laser power is varied with fixed $\Omega_P = 2\pi \times 3.5$ MHz.

vary them to determine the optimal conditions for detecting weak rf E fields. Because total absorption scales with probe laser intensity, larger Ω_P typically leads to larger pulse depths, and therefore, larger matched-filter signals. However, our photodetector saturates at large probe powers, requiring the addition of a neutral density filter in front of the detector. Thus, for better comparison in Fig. 7(c), we normalize the matched-filter peak height at a given Ω_P to its value at large rf E fields, both averaged over 300 cycles. This maps changes in EIT peak width and overlap as a function of rf amplitude and Ω_P, for fixed $\Omega_C = 2\pi \times 2.4$ MHz. At small Ω_P, the EIT peaks are spectrally narrower, so that the Autler-Townes regime is extended and a lower rf E field can be reached before the peaks begin to overlap and pulse amplitude decreases. If the aim is to maximize sensitivity to weak rf E fields, then lower Ω_P is desirable. In contrast, if the aim is to differentiate a wide range of rf E-field amplitudes, then larger Ω_P is preferable because the pulse depth varies gradually with rf E-field amplitude due to broad overlapping EIT peaks.

Figure 7(d) shows changes in SNR as Ω_C is varied while $\Omega_P = 2\pi \times 3.5$ MHz. For analysis of the matched filter's performance, we define the SNR by taking an average of matched-filter peak heights from 300 pulse traces then dividing by the standard deviation of noise measured from 300 traces of identical length taken with no rf E field present. If a pulse cannot be identified within a given trace, i.e., there is a missed detection or larger false alarm from a mistimed noise spike, then we set the detected height for that trace to zero. Each trace is at least 10 times longer duration than an individual pulse to capture false alarms and provide a more realistic SNR. Reducing Ω_C improves the SNR at the lowest rf E fields by spectrally narrowing the EIT peaks but comes at the cost of a reduced SNR at high-rf E fields due to lower EIT peak amplitude. At this Ω_P, further reductions in coupling Rabi frequency beyond $\Omega_C \sim 2\pi \times 0.9$ MHz are detrimental to the SNR at all rf E fields.

In Fig. 8, we investigate detection performance for pulses with different lengths under laser conditions that give the overall highest SNR, $\Omega_P = 2\pi \times 3.5$ MHz and $\Omega_C = 2\pi \times 2.1$ MHz. We evaluate the timing precision as the standard deviation of a Gaussian fit to a distribution of 300 pulse timings extracted in postprocessing from the matched-filter maxima. Timing precision and the SNR for weak rf fields are limited by a small atomic response depth.
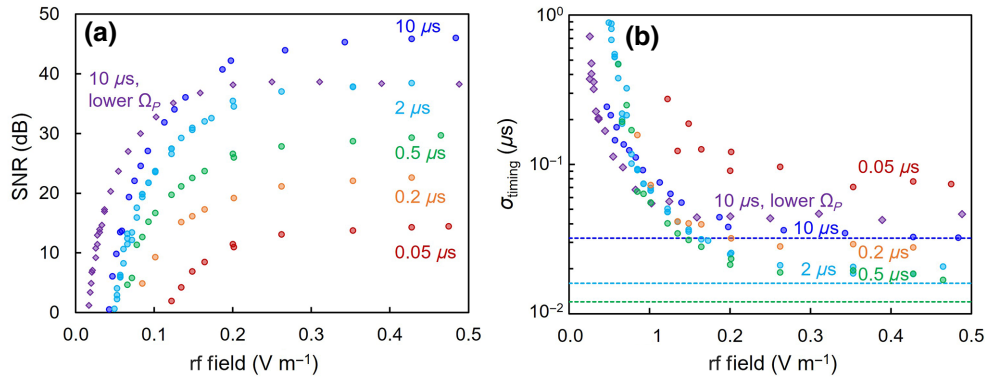
FIG. 8. (a) SNR of the matched filter shown for various rf-pulse lengths (circles) and for 10-μs pulses taken at a lower IR power of $\Omega_P = 2\pi \times 1.7$ MHz instead of $\Omega_P = 2\pi \times 3.5$ MHz. (b) Timing precision for the various pulse conditions in (a), taken as the standard deviation of a Gaussian fit to pulse timings measured from the matched-filter peak. Dashed horizontal lines correspond to hardware limits due to the finite sampling rate of the FPGA implementing the matched filter.

At larger rf E-fields, timing precision can be limited by the downsampling required to implement the matched filter on the FPGA. Limits from the sampling rate are indicated as horizontal dashed lines in Fig. 8(b), which generally can be increased for shorter pulses.

If the EIT peaks are fully split, then the SNR remains constant with varying rf E field but drops once overlap occurs at weaker rf E fields. At a SNR of about 15 dB, we begin to see rare false alarms ($<1\%$), which increase at lower SNRs. Pulses shorter than 0.5 μs do not have time to reach sufficient depth because of the finite atomic response time [Fig. 1(d)], which degrades the SNR and timing precision at all rf amplitudes. Despite this, we are able to detect individual short pulses with the matched filter, down to the rf generator's 50-ns width limit.

Using optimal laser conditions for detecting weak rf pulses (purple), $\Omega_P = 2\pi \times 1.7$ MHz and $\Omega_C = 2\pi \times 2.1$ MHz, our rf E-field sensitivity reaches about 170 μV cm^{-1} when the SNR is about 0 dB. For a 2-μs sensing time, this corresponds to a sensitivity of approximately 240 nV cm^{-1} Hz$^{-1/2}$. When the SNR approaches 15 dB and occasional false alarms become apparent, corresponding to a rf E-field limit of about 330 μV cm^{-1}, a 2-μs sensing time yields an effective sensitivity of 470 nV cm^{-1} Hz$^{-1/2}$. These sensitivities are obtained in real time on single pulses, without the need for an auxiliary reference rf E field, averaging, or additional modulation.

V. USE OF BURST RF-PULSE SEQUENCES

We also investigate the application of the FPGA-implemented matched filter to short bursts of rf pulses to improve detection. We use a series of three 2-μs pulses spaced by 2 μs, so that the total pattern is 10-μs long

but contains lower total energy than that of a single 10-μs pulse. The template used for the matched filter is shown in Fig. 9(a), and the output on a typical noisy experimental pulse is given in Fig. 9(b).

When the matched-filter template is well matched to the incoming pulse waveform, $x(t)$, and the noise is Gaussian with a noise power spectral density of σ^2 in units of W/Hz, the expected SNR is given by [38]

$$\text{SNR} = \frac{E}{\sigma^2} = \frac{\int_{-\infty}^{\infty} |x(t)|^2 dt}{\sigma^2}. \tag{7}$$

This depends only on the energy, E, of the waveform. If we consider perfect square pulses with identical amplitude and Gaussian-noise characteristics, then the detection of a single 10-μs-long square pulse will have 5 times the SNR of a single 2-μs-long pulse due to the longer pulse duration. If we were to detect a series of three 2-μs long pulses, then the SNR would be 3 times that of the single 2-μs-long pulse. Despite the deviation in the atomic response from a square pulse, this is close to what is observed experimentally in Fig. 9(c). At high-rf E fields, a 10-μs pulse produces a SNR that is typically 5.5 times that of a single 2-μs pulse, while a burst pattern of three 2-μs-long pulses produces a SNR 3.6 times that of a single 2-μs pulse. However, we find that, due to the addition of side lobes in the matched-filter pattern, the use of burst sequences comes with an added false timing rate of about 5%, resulting from the cases where the side lobe exceeds the central peak due to noise. At low-rf electric fields, the same physical picture applies, but the matched filter is more sensitive to variations in the pulse shape and depth that depend on the measurement parameters.

Although the burst pattern is not advantageous over a single long pulse in terms of the SNR, it produces a narrower peak in the matched-filter output, which can improve timing precision. This can be intuitively understood using
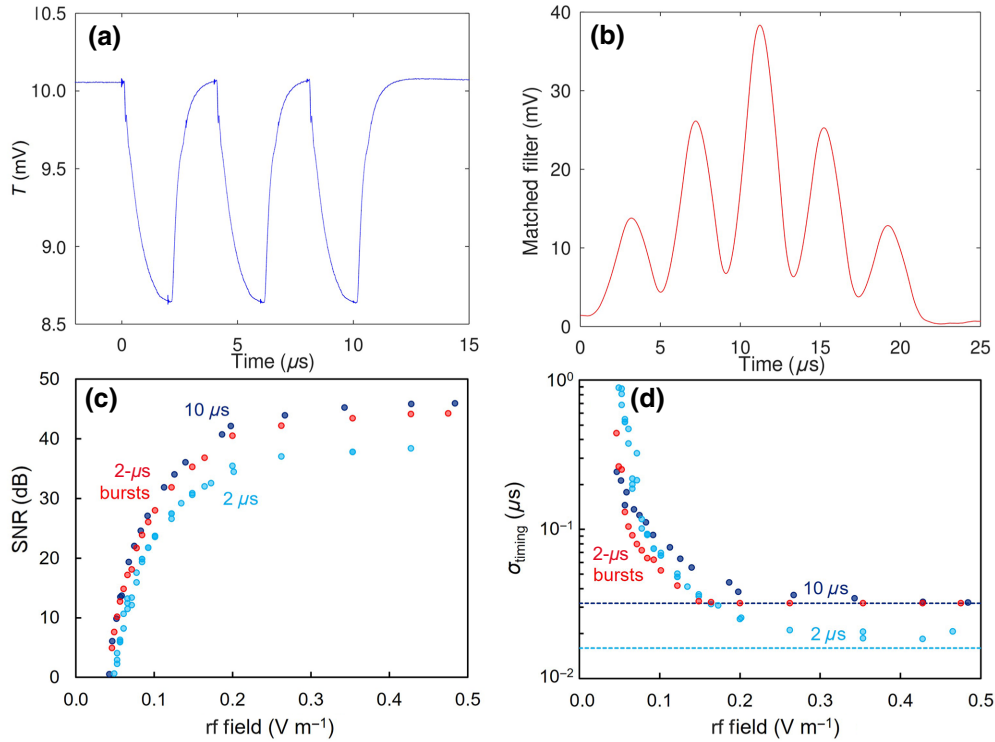
FIG. 9. Use of a burst sequence to improve pulse detection. (a) Averaged atomic response to a series of three 2-μs rf pulses spaced by 2 μs, forming the template for the matched filter. (b) Application of the matched filter to a single noisy burst sequence produces an output with a narrower central peak that is less prone to timing inaccuracy at weak rf E fields, but with additional side lobes that can lead to false alarms. (c) Bursts (red) show a SNR between that of a single 10-μs pulse (dark blue) and a single 2-μs pulse (light blue). (d) Burst sequences demonstrate improved timing accuracy over single pulses.

the following picture, although a quantitative description of the expected improvement is nontrivial [39]. The time at which the peak of the matched filter occurs serves as an indicator of pulse arrival time, and here we treat the peak to be simply the maximum of the matched-filter output signal, which occurs at a time t_{PK} if there is no noise. In the presence of noise fluctuations with an average amplitude σ, the timing precision can be thought of as limited by the furthest away in time at which a jump of amplitude σ can cause the signal to exceed the maximum at t_{PK} with significant probability. If the matched filter is broad, i.e., it has a small slope near t_{PK}, then there is a large range in time over which a σ noise fluctuation can cause a new maximum, resulting in worse timing precision. For a single square pulse of amplitude A, the slope of the triangular matched-filter output will be A^2, which is independent of the pulse duration. For a burst pattern consisting of N square pulses of amplitude A, the central triangular peak in the matched-filter output will be steeper with a slope of NA^2. Thus, the timing precision of a burst pattern in the presence of noise is expected to exceed that of either a single 2- or 10-μs pulse. Experimentally, we observe that, at low-to-moderate rf fields, the use of the burst pattern improves timing precision by about 33% over a single longer 10-μs pulse (at high-rf fields, timing precision is limited by the

hardware). Further improvements can be achieved by varying the amplitude of each pulse in the sequence based on compression techniques [40,41].

VI. NONLINEARITY AND MATCHED-FILTER TEMPLATE MISMATCH

Using the matched filter implies a linear time-invariant system, but the atomic system is nonlinear and time varying. Given that the template is by necessity preassigned and unable to respond in real time to changing conditions, the consequence is that there may be a mismatch between the pulse shape and template, altering the extracted pulse arrival time and SNR.

In Fig. 10(a), we examine how the pulse shape changes nonlinearly with rf E-field amplitude. For a large range of rf E fields, we find that the pulse shape remains largely the same, with only a subtle change to the slower time constant after the initial transient. However, once the amplitude regime is reached at low-rf E fields, below about 0.1 V m^{-1}, both edges of the pulse develop overshoots due to Rabi oscillations associated with the fast transient. The atoms are more sensitive to fluctuations in amplitude from the rf generator at weak rf E fields, i.e., in the sloped
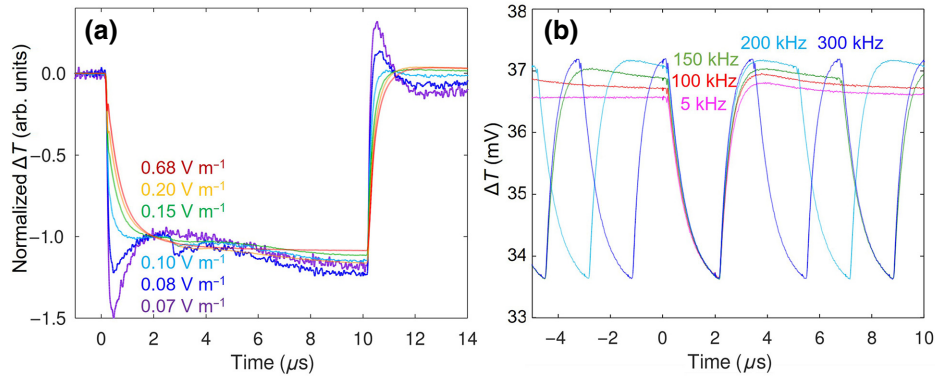
FIG. 10. (a) Pulse shape at different rf E fields, normalized to the same depth. At weaker fields, the atomic response is slightly more rapid, and as the rf E-field amplitude is further decreased, overshoots begin to develop on each edge. $\Omega_P = 2\pi \times 3.5$ MHz, $\Omega_C = 2\pi \times 2.1$ MHz. (b) Effects of repetition rate on pulse shape for 2-μs-long pulses. $\Omega_P = 2\pi \times 8.8$ MHz, $\Omega_C = 2\pi \times 2.1$ MHz, $\Omega_{rf} = 2\pi \times 120$ MHz.

regions of Fig. 7(c), resulting in an atomic response that is not flat between about 2.5 and 10 μs.

The shape of the atomic response can also vary with the pulse repetition rate due to collisions, ionization, and electric field effects with substantially longer equilibration timescales than a single pulse. Figure 10(b) shows that the pulse depth and timescales vary slightly with pulse rate. In particular, when the pulse repetition rate is low and dark-state atoms or ions have time to accumulate, then an overshoot is present on the tail of the pulse.

In Fig. 11, we demonstrate what happens if the matched-filter template (red inset) is not a perfect match to the underlying pulse shape being detected (blue inset). This can arise primarily from the nonlinearity and time variance of the atomic system, but may also occur due to changes in the vapor cell itself (e.g., electric fields, vapor pressure) or

the lasers (e.g., power, frequency detuning). For this analysis, we perform matched-filter computations in postprocessing on averaged data rather than that implemented for real-time analysis on the FPGA hardware to avoid shifts due to noise. We find that differences in the timescales comprising the pulse, or the presence of overshoots on the edges, result in slight shifts to the pulse time extracted at the maximum of the filter output that are generally <0.5 μs for a 10-μs-long pulse. The direction of the shift can be later or earlier, depending on the nature of the pulse-template mismatch. The symmetric presence of overshoots on the leading and trailing edges of the pulse helps to mitigate any shift due to differences in rf amplitude, but detection can be improved by using two filters run in parallel, one designed for large rf amplitudes and another for small rf amplitudes. On the other hand, temporal variation can be minimized by working in a weak-field EIT limit,
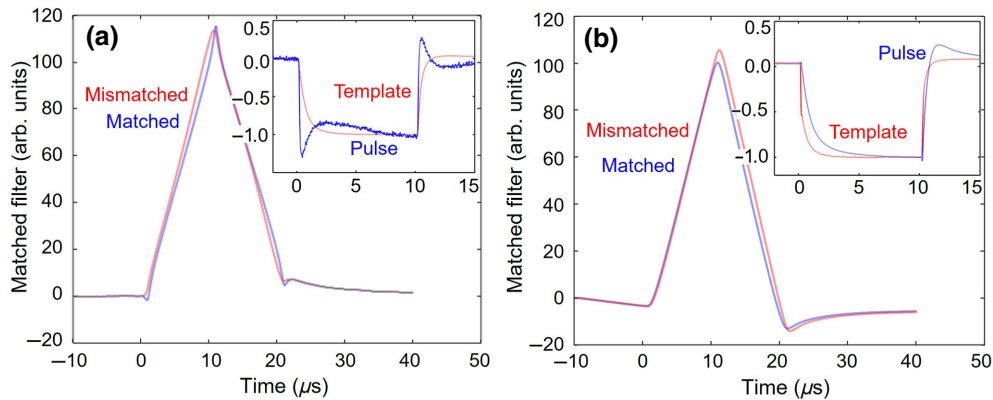
FIG. 11. Using a template that does not fully match the atomic pulse shape produces slight shifts in the extracted pulse timing from the matched filter (red) compared to using an ideal match (blue). Insets show the shapes of the template (red) and target pulse (blue). (a) Pulse template for large rf E-field amplitudes is used on a weak rf E-field atomic response. (b) Scenario where the target pulse contains unanticipated strong collisional, ionization, and electric field effects on the tail.
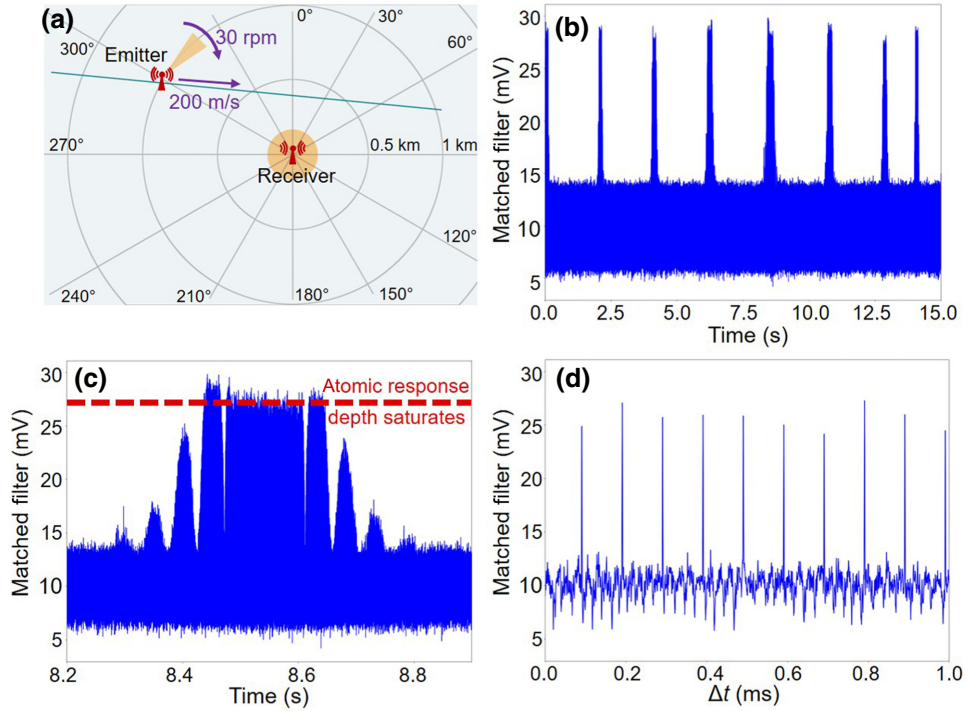
FIG. 12. Radar detection. (a) Scenario describing a rotating emitter on an aircraft as it flies past a fixed vapor cell receiver, emitting 1-μs pulses at a repetition frequency of 10 kHz. (b) Detected signal after matched filtering, producing clusters of pulses whenever the emitter's antenna rotates to face the receiver. (c) Magnification of a pulse cluster shows the pattern formed from a single rotation of the antenna, consisting of a large central peak with multiple weaker side lobes. Central lobes appear flat due to saturation of the atomic-pulse-response depth at high-rf E fields. (d) Further magnification of the central lobe at 8.5 s shows the matched-filter output from individual 1-μs pulses. $\Omega_P = 2\pi \times 1.7$ MHz, $\Omega_C = 2\pi \times 2.1$ MHz.

i.e., with Rabi frequencies chosen for low Rydberg-state populations.

VII. RADAR DETECTION AND DISCUSSION

Finally, we demonstrate the experimental detection of emulated radar signals from an aircraft flying past our vapor cell receiver with a path shown in Fig. 12(a). The signal is produced by a vector signal generator that simulates the power and timing of pulses that reach the receiver, accounting for changing distance, which we send to the rf horn antenna near the vapor cell. The simulated aircraft travels at a typical commercial airplane speed of 200 m/s at a distance of around 1 km from the receiver. On board is a spinning antenna rotating at 30 rpm (rotates once every 2 s), emitting 1-μs-long pulses at a repetition rate of 10 kHz. The simulated emitter is a pyramidal horn with dimensions of 12.7×9.4 cm^2, with an 8° beamwidth in the scan plane, and the rf field falls off with distance as $1/r$. The result is a peak rf E field received at the vapor cell of around 1.05 V m^{-1} at the point of closest approach. For detection, we use laser conditions corresponding to the highest rf E-field sensitivity, with $\Omega_P = 2\pi \times 1.7$ MHz and $\Omega_C = 2\pi \times 2.1$ MHz.

Figure 12(b) shows the radar pattern seen through the atomic response of the vapor cell, processed with the FPGA-implemented matched filter. Clusters of pulses are visible when the emitter faces the receiver, the amplitudes of which vary in an antenna pattern [Fig. 12(c)]. However, due to the atomic nonlinearity and saturation at high-rf amplitudes [see Fig. 7(c)], the central lobes appear flat rather than rounded like the side lobes. Furthermore, the first side lobe has a slightly higher amplitude than the central lobe due to the enhanced absorption on the sides of the EIT peak under these laser conditions. As the aircraft approaches the receiver, the rf E field at the vapor cell increases, and more side lobes can be distinguished above the noise floor. However, the central lobe heights do not change due to atomic-pulse-depth saturation.

In radar applications, improved timing precision translates into increased spatial resolution of a target's location. For instance, the timing uncertainty of about 30 ns demonstrated in this work corresponds to 9-m uncertainty in the distance to the emitter (or 4.5-m uncertainty in the target location if the emitter is located at the receiver and the radar signal is reflected off the target). Relative to the typical distances over which radar is used, on the order of kilometers, and the size of a target, such as an airplane,

such an uncertainty is small. As this timing precision is sufficient, remaining challenges for implementing this technology are to improve sensitivity for distinguishing targets at weaker rf E-field amplitudes. This either increases the radar range over which a target can be detected or allows one to reduce energy requirements of the emitter. To detect a target from further away or distinguish weaker rf amplitudes, an increase in emitted pulse length, an increase in vapor cell depth, addition of an amplifier at the receiver (e.g., a dish), a reduction in noise sources, or averaging over several pulses is required.

Although Rydberg-atom-based sensors are sometimes said to measure power, they actually measure electric field strength, E, and ideally do not dissipate energy or perturb the incident field. The closest power measurement is power density, P_D (W/m²), given by $P_D = E^2/Z_0$, where $Z_0 = 377\ \Omega$, considering the detector is placed in free space, as assumed in this work. The absolute power, P, can then be obtained by multiplying P_D by the atom-absorption cross section, $3\lambda^2/2\pi$, since each atom is an independent sensor. An electric field sensitivity of $240\ \mathrm{nV\ cm^{-1}\ Hz^{-1/2}}$ at 20 GHz ($\lambda = 1.5$ cm), therefore, corresponds to a power-density sensitivity of $1.5 \times 10^{-12}\ \mathrm{W\ m^{-2}\ Hz^{-1}}$ and a power sensitivity of $1.6 \times 10^{-16}\ \mathrm{W\ Hz^{-1}}$. In a 1-Hz bandwidth, this is -128 dBm, and if we use a 2-MHz bandwidth, then the minimum power detectable is -71 dBm.

For context, the thermal noise floor (at 20 °C) in a 1-Hz bandwidth is approximately -174 dBm (and -117 dBm in a 2-MHz bandwidth). In comparison, the typical thermal noise floor for the Global Positioning System in a 2-MHz bandwidth is about -111 dBm, while a state-of-the-art room-temperature receiver based on a Schottky diode has a sensitivity of about $4 \times 10^{-19}\ \mathrm{W\ Hz^{-1}}$ [42,43]. These numbers seem to indicate that the Rydberg-atom system has poor sensitivity, but one must realize that the experimental numbers presented here are not optimal and are quoted without any collection optics. If we use a 1-m² dish, then the power sensitivity goes to $1.6 \times 10^{-20}\ \mathrm{W\ Hz^{-1}}$, which is -168 dBm (-111 dBm) in a 1-Hz (2-MHz) bandwidth. By approaching the shot noise limit of about $30\ \mathrm{nV\ cm^{-1}\ Hz^{-1/2}}$ and engineering the vapor cells [44], even higher sensitivity can be obtained.

Although doing experiments with a dish or the vapor cells mentioned is outside the scope of this work, it is nevertheless relevant to explore pulse detection with Rydberg atoms for radar, since these receivers have advantages such as broad bandwidth, dielectric construction, and self-calibration, which make them unique, while promising to compete in sensitivity. Pulsed detection is necessary for radar and communications applications, since modulation of the field in amplitude, phase, frequency, or polarization is necessary to encode signals and determine the properties of targets.

VIII. CONCLUSION

We show that a room-temperature Cs vapor cell has a rapid response to pulse-modulated rf E fields and can detect rf pulses down to sub-50-ns durations. The overall atomic response time consists of two timescales: a short about-100-ns transient followed by a longer microsecond decay that depends on the transit time of Rydberg atoms and collisional byproducts out of the interaction region. Using a matched filter based on the atomic response, we find that the vapor cell can detect single-shot rf pulses down to amplitudes of about $170\ \mu\mathrm{V\ cm^{-1}}$, with a sensitivity of about $240\ \mathrm{nV\ cm^{-1}\ Hz^{-1/2}}$ and timing precision of about 30 ns without the use of an auxiliary field or other signal processing. We find that weak-laser conditions are optimal for the highest sensitivity to low-rf amplitudes, while higher laser powers are preferred for distinguishing a broader amplitude range. Finally, we demonstrate the functionality of Rydberg-atom-based sensors as a radar receiver, detecting pulses emitted by an aircraft antenna.

[1] C. S. Adams, J. D. Pritchard, and J. P. Shaffer, Rydberg atom quantum technologies, J. Phys. B: At., Mol. Opt. Phys. **53**, 012002 (2019).

[2] H. Weimer, M. Müller, I. Lesanovsky, P. Zoller, and H. P. Büchler, A Rydberg quantum simulator, Nat. Phys. **6**, 382 (2010).

[3] I. M. Georgescu, S. Ashhab, and F. Nori, Quantum simulation, Rev. Mod. Phys. **86**, 153 (2014).

[4] M. Saffman, Quantum computing with atomic qubits and Rydberg interactions: Progress and challenges, J. Phys. B: At., Mol. Opt. Phys. **49**, 202001 (2016).

[5] L. Henriet, L. Beguin, A. Signoles, T. Lahaye, A. Browaeys, G.-O. Reymond, and C. Jurczak, Quantum computing with neutral atoms, Quantum **4**, 327 (2020).

[6] Ripka Fabian, Kübler Harald, Löw Robert, and Pfau Tilman, A Room-temperature single-photon source based on strongly interacting Rydberg atoms, Science **362**, 446 (2018).

[7] J. A. Sedlacek, A. Schwettmann, H. Kübler, R. Löw, T. Pfau, and J. P. Shaffer, Microwave electrometry with Rydberg atoms in a vapour cell using bright atomic resonances, Nat. Phys. **8**, 819 (2012).

[8] C. L. Holloway, J. A. Gordon, S. Jefferts, A. Schwarzkopf, D. A. Anderson, S. A. Miller, N. Thaicharoen, and G. Raithel, Broadband Rydberg atom-based electric-field probe for SI-traceable, self-calibrated measurements, IEEE Trans. Antennas Propag. **62**, 6169 (2014).

[9] H. Fan, S. Kumar, J. Sedlacek, H. Kübler, S. Karimkashi, and J. P. Shaffer, Atom based rf electric field sensing, J. Phys. B: At., Mol. Opt. Phys. **48**, 202001 (2015).

[10] C. L. Holloway, M. T. Simons, J. A. Gordon, P. F. Wilson, C. M. Cooke, D. A. Anderson, and G. Raithel, Atom-based rf electric field metrology: From self-calibrated measurements to subwavelength and near-field imaging, IEEE Trans. Electromagn. Compat. **59**, 717 (2017).

[11] M. T. Simons, A. B. Artusio-Glimpse, A. K. Robinson, N. Prajapati, and C. L. Holloway, Rydberg atom-based sensors for radio-frequency electric field metrology, sensing, and communications, Meas. Sens. **18,** 100273 (2021).

[12] J. Gea-Banacloche, Y. Li, S. Jin, and M. Xiao, Electromagnetically induced transparency in ladder-type inhomogeneously broadened media: Theory and experiment, Phys. Rev. A **51,** 576 (1995).

[13] M. Fleischhauer, A. Imamoglu, and J. P. Marangos, Electromagnetically induced transparency: Optics in coherent media, Rev. Mod. Phys. **77,** 633 (2005).

[14] S. Kumar, H. Fan, H. Kübler, A. J. Jahangiri, and J. P. Shaffer, Rydberg-atom based radio-frequency electrometry using frequency modulation spectroscopy in room temperature vapor cells, Opt. Express **25,** 8625 (2017).

[15] J. P. Shaffer and H. Kübler, in A read-out enhancement for microwave electric field sensing with Rydberg atoms, (2018), Vol. 10674.

[16] S. Kumar, H. Fan, H. Kübler, J. Sheng, and J. P. Shaffer, Atom-based sensing of weak radio frequency electric fields using homodyne readout, Sci. Rep. **7,** 42981 (2017).

[17] M. Jing, Y. Hu, J. Ma, H. Zhang, L. Zhang, L. Xiao, and S. Jia, Atomic superheterodyne receiver based on microwave-dressed Rydberg spectroscopy, Nat. Phys. **16,** 911 (2020).

[18] H. Q. Fan, S. Kumar, R. Daschner, H. Kübler, and J. P. Shaffer, Subwavelength microwave electric-field imaging using Rydberg atoms inside atomic vapor cells, Opt. Lett. **39,** 3030 (2014).

[19] F. Ripka, H. Amarloo, J. Erskine, C. Liu, J. Ramirez-Serrano, J. Keaveney, G. Gillet, H. Kübler, and J. P. Shaffer, in Application-driven problems in Rydberg atom electrometry, (2021), Vol. 11700.

[20] R. E. Sapiro, G. Raithel, and D. A. Anderson, Time dependence of Rydberg EIT in pulsed optical and rf fields, J. Phys. B: At., Mol. Opt. Phys. **53,** 094003 (2020).

[21] D. H. Meyer, K. C. Cox, F. K. Fatemi, and P. D. Kunz, Digital communication with Rydberg atoms and amplitude-modulated microwave fields, Appl. Phys. Lett. **112,** 211108 (2018).

[22] D. A. Anderson, R. E. Sapiro, and G. Raithel, An atomic receiver for AM and FM radio communication, IEEE Trans. Antennas Propag. **69,** 2455 (2021).

[23] Y. Jiao, X. Han, J. Fan, G. Raithel, J. Zhao, and S. Jia, Atom-based receiver for amplitude-modulated baseband signals in high-frequency radio communication, Appl. Phys. Express **12,** 126002 (2019).

[24] C. Holloway, M. Simons, A. H. Haddab, J. A. Gordon, D. A. Anderson, G. Raithel, and S. Voran, A multiple-band Rydberg atom-based receiver: AM/FM stereo reception, IEEE Antennas Propag. Mag. **63,** 63 (2021).

[25] Z. Song, H. Liu, X. Liu, W. Zhang, H. Zou, J. Zhang, and J. Qu, Rydberg-atom-based digital communication using a continuously tunable radio-frequency carrier, Opt. Express **27,** 8848 (2019).

[26] M. T. Simons, A. H. Haddab, J. A. Gordon, and C. L. Holloway, A Rydberg atom-based mixer: Measuring the phase of a radio frequency wave, Appl. Phys. Lett. **114,** 114101 (2019).

[27] D. A. Anderson, R. E. Sapiro, and G. Raithel, Rydberg atoms for radio-frequency communications and sensing: Atomic receivers for pulsed rf field and phase detection, IEEE Aerosp. Electron. Syst. Mag. **35,** 48 (2020).

[28] S. Krämer, D. Plankensteiner, L. Ostermann, and H. Ritsch, QuantumOptics. Jl: A Julia framework for simulating open quantum systems, Comput. Phys. Commun. **227,** 109 (2018).

[29] D. Manzano, A short introduction to the Lindblad master equation, AIP Adv. **10,** 025106 (2020).

[30] D. A. Steck, Cesium D line data (2003).

[31] M. Newville, T. Stensitzki, D. B. Allen, and A. Ingargiola, LMFIT: Nonlinear least-square minimization and curve-fitting for PYTHON (2014).

[32] R. Storn and K. Price, Differential evolution—a simple and efficient heuristic for global optimization over continuous spaces, J. Glob. Optim. **11,** 341 (1997).

[33] A. Schwettmann, J. Crawford, K. R. Overstreet, and J. P. Shaffer, Cold Cs Rydberg-gas interactions, Phys. Rev. A **74,** 020701 (2006).

[34] D. Weller, J. P. Shaffer, T. Pfau, R. Löw, and H. Kübler, Interplay between thermal Rydberg gases and plasmas, Phys. Rev. A **99,** 043418 (2019).

[35] I. I. Beterov, D. B. Tretyakov, I. I. Ryabtsev, V. M. Entin, A. Ekers, and N. N. Bezuglov, Ionization of Rydberg atoms by blackbody radiation, New J. Phys. **11,** 013052 (2009).

[36] L. Barbier and M. Cheret, Experimental study of Penning and Hornbeck-Molnar ionisation of rubidium atoms excited in a high s or d level ($5d \leq nl \leq 11s$), J. Phys. B: At. Mol. Phys. **20,** 1229 (1987).

[37] J. Huennekens, Z. Wu, and T. G. Walker, Ionization, excitation of high-lying atomic states, and molecular fluorescence in Cs vapor excited at $\Lambda = 455.7$ and 459.4 Nm, Phys. Rev. A **31,** 196 (1985).

[38] M. A. Richards, in *Fundamentals of Radar Signal Processing*, 2nd ed. (McGraw-Hill, New York, 2014).

[39] D. J. Torrieri, The uncertainty of pulse position due to noise, IEEE Trans. Aerosp. Electron. Syst. **AES-8,** 661 (1972).

[40] B. M. Keel, in *Principles of Modern Radar*, edited by M. A. Richards, J. A. Scheer, and W. A. Holm (SciTech Publishing, Raleigh, NC, 2010).

[41] F. F. Kretschmer Jr and F. C. Lin, *Huffman-Coded Pulse Compression Waveforms* (Naval Research Lab, Washington DC, 1985).

[42] T. W. Crowe, R. J. Mattauch, H. P. Roser, W. L. Bishop, W. C. B. Peatman, and X. Liu, GaAs Schottky diodes for THz mixing applications, Proc. IEEE **80,** 1827 (1992).

[43] T. Nagatsuma, G. Ducournau, and C. C. Renaud, Advances in terahertz communications accelerated by photonics, Nat. Photonics **10,** 371 (2016).

[44] H. Amarloo, J. Ramirez-Serrano, and J. P. Shaffer, Photonic crystal receivers, 11,137,432 (2021).